Low-Fidelity 2D Isogeometric Aeroelastic Analysis and Optimization Method with Application to a Morphing Airfoil

Gillebaart, Erik; De Breuker, Roeland

DOI
10.1016/j.cma.2016.03.014

Publication date
2016

Document Version
Accepted author manuscript

Published in
Computer Methods in Applied Mechanics and Engineering

Low-Fidelity 2D Isogeometric Aeroelastic Analysis and Optimization Method with Application to a Morphing Airfoil

E. Gillebaart[a,*], R. De Breuker[a]

[a]*Department of Aerospace Structures and Computational Mechanics, Faculty of Aerospace Engineering, Delft University of Technology*

Abstract

Low-fidelity isogeometric aeroelastic analysis has not received much attention since the introduction of the isogeometric analysis (IGA) concept, while the combination of IGA and the boundary element method in the form of the potential flow theory shows great potential. This paper presents a two-dimensional low-fidelity aeroelastic analysis and optimization framework consisting of a closely coupled isogeometric potential flow model and isogeometric curved Timoshenko beam model combined with a boundary layer model. Application of the framework to the optimization of the landing performance for an active morphing airfoil demonstrates the potential of the isogeometric aeroelastic framework.

Keywords: Isogeometric analysis, Aeroelasticity, Morphing airfoil, Optimization

1. Introduction

Isogeometric analysis (IGA) has captured the attention of many researchers in the past decade. The principle of IGA, introduced in 2005 [1], is to apply basis functions that are typically used in computer aided design (CAD) to the analysis as well, instead of the conventional polynomial basis functions. The main benefit of this approach is that the step from CAD geometry to an analysis suitable geometry is largely circumvented, since the CAD geometry can directly be used in the analysis. This also greatly simplifies mesh refinement and degree elevation, as the coarsest mesh is already the exact geometry. For an overview of IGA and its application, see the work by Nguyen et al. [2]

The application of IGA in the field of aeroelasticity and fluid-structure interaction (FSI) has been limited so far and is usually focused on high-fidelity modeling using, for example, fluid models based on the Navier-Stokes equations and non-linear structural shell models. Most of the contributions come from Bazilevs and his team. Two main subjects are FSI of wind turbines and arterial blood flows. The work on wind turbines is based on incompressible Navier-Stokes and non-linear Kirchhoff-Love shell elements supported by bending strips, using either matching [3] or non-matching [4, 5] discretizations. The non-matching discretization consists of, for example, a T-spline shell model and a conventional finite element fluid model. The work on arterial blood flows is also based on incompressible Navier-Stokes, but uses non-linear solids to model the arterial walls [6, 7]. The high computational cost related to these fluid and structural models prohibits their use in optimization routines.

Low-fidelity models, although having a somewhat lower accuracy, can enable the use of extensive optimization in early design stages. Low-fidelity aeroelastic analysis has been almost untouched to the authors' knowledge, while, for example, aerodynamic analysis in the form of the boundary element method (BEM) has been shown to be a suitable candidate for the implementation of IGA. The work of Politis et al. showed the application of IGA to exterior planar Neumann potential problems and they demonstrated superior

*Corresponding author.
Address: Kluyverweg 1, 2629 HS Delft, The Netherlands.
Email address: e.gillebaart@tudelft.nl

convergence properties compared to a conventional BEM implementation [8]. Takahashi and Matsumoto demonstrated the application of the fast multipole method to the same type of problem, reducing the computational cost from quadratic to linear with respect to the number of control points [9]. One of the most important challenges in BEM, computing the singular integrals, was tackled by Heltai et al. by desingularizing the boundary integral equation. The application to 3D Stokes flow problems showed the accuracy of the method [10].

The fact that the BEM only requires a boundary description of the problem creates a perfect match with CAD, since the output of such software is only a boundary discretization. Furthermore, analyzing the exact geometry is beneficial for aerodynamic analysis, since small perturbations can have significant effects. Also in other fields it has been shown that the benefits of IGA work well in a BEM framework. Simpson et al. applied IGA to 2D elastostatic analysis [11] and later to acoustics, using T-splines instead of non-uniform rational b-splines (NURBS) [12]. The elastostatic analysis was expanded to multipatch 3D analysis in the work of Lian et al. [13]. Scott et al. used T-spline instead of NURBS in 3D elastostatic analysis [14].

Another advantage of IGA is that it is very suitable for shape optimization problems, especially in a BEM framework, as has been shown for structural shape optimization in 2D, using a desingularized BEM formulation, by Lian et al. [15] and in 3D by Li and Qian [16]. The IGA implementation delivers very accurate shape sensitivities, resulting in precise optimization results. Furthermore, the discretization can be used directly in optimization, removing the need for a separate shape parametrization as demonstrated by Cho and Ha [17].

All these benefits of IGA have lead to the idea of implementing the concept into a low-fidelity aeroelastic framework with the purpose of performing simultaneous shape and stiffness optimization of composite wings during the preliminary design phase. The performance increase resulting from this simultaneous optimization has been shown already using high- fidelity aeroelastic frameworks [18], but these are computationally expensive, making them less attractive for the early design stages.

As a first step, this paper presents a two-dimensional low-fidelity aeroelastic framework based on the IGA concept. An IGA potential flow solver is closely coupled to an IGA curved Timoshenko beam solver formulated in a global reference system. Subsequently, a one-way coupling is formed between the aeroelastic model and a boundary layer model. A gradient-based optimizer is used in combination with sensitivities computed using algorithmic differentiation. To show the capabilities of the framework, it is applied to the aeroelastic optimization of an active morphing airfoil.

The paper is built up as follows. In section 2 a short introduction into IGA is given, and the aerodynamic, structural and boundary layer models are described. The coupling of the models is also explained. The next section presents the design case of the morphing airfoil, together with the optimization specifications. The results are presented and discussed in section 4 and the paper is concluded in section 5.

2. Methodology

The low-fidelity aeroelastic framework consists of an isogeometric potential flow aerodynamic model and an isogeometric curved Timoshenko beam structural model. This section will describe the theory and implementation of both these models. The coupling between these models and the loads and displacements transfer method will also be presented. First a short introduction into NURBS and isogeometric analysis is given for completeness.

2.1. NURBS curves and basis functions

In the present work NURBS basis functions are used, because these are the most common in CAD software. A NURBS curve is fully defined by three items:

- The control points $\mathbf{P}_i \in \mathbb{R}^d, 1 \leq i \leq n$, where d indicates the dimensionality of the problem.
- The degree p of the basis functions.
- The knot vector $\Xi = [\xi_1, \xi_2, ..., \xi_{n+p+1}]$.

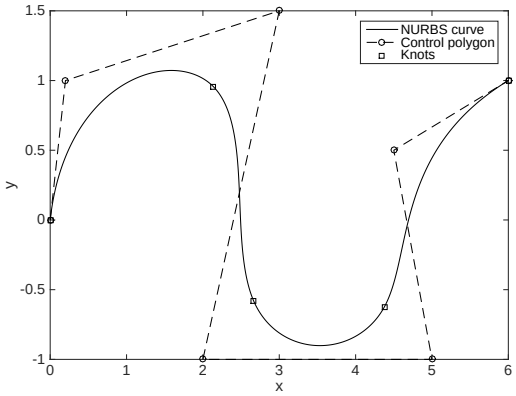

Figure 1: Example of a NURBS curve with control polygon and knot location

An example of a two-dimensional NURBS curve of degree 3 is shown in Figure 1. From this example it can be seen that the control point may or may not be on the curve. Only so-called open knot vectors are used in the present work, meaning that the first and last knots are repeated $p+1$ times. As a consequence the NURBS curve is always interpolatory at the start and end of the curve. The order of continuity of the rest of the curve can be modified by repeating the other knots. The order of continuity at a knot is equal to $p+1-r$, where r is the multiplicity of this knot.

Mathematically a NURBS curve can be represented as follows:

$$\mathbf{C}(\xi) = \sum_{i=1}^{n} R_{i,p}(\xi)\mathbf{P}_i \tag{1}$$

where $\mathbf{C}(\xi)$ is the vector with Cartesian coordinates of the point described by the parametric point $\xi_1 \leq \xi \leq \xi_{n+p+1}$, and $R_{i,p}(\xi)$ is the i^{th} rational basis functions of degree p. These basis functions are given by

$$R_{i,p}(\xi) = \frac{N_{i,p}(\xi)w_i}{\sum_{j=1}^{n} N_{j,p}(\xi)w_j} \tag{2}$$

where $N_{i,p}(\xi)$ is a B-spline basis function of order p, and w_i is the weight factor corresponding to the i^{th} control point. The B-spline basis functions of degree 0 are defined as

$$N_{a,0}(\xi) = \begin{cases} 1 & \text{if } \xi_i \leq \xi \leq \xi_{i+1} \\ 0 & \text{otherwise} \end{cases} \tag{3}$$

and for higher degrees

$$N_{i,p}(\xi) = \frac{\xi - \xi_i}{\xi_{i+p} - \xi_i} N_{i,p-1}(\xi) + \frac{\xi_{i+p+1} - \xi}{\xi_{i+p+1} - \xi_{i+1}} N_{i+1,p-1}(\xi) \tag{4}$$

The recursive character results in higher cost for computing the basis functions. However, several efficient algorithms exist to speed up the computations, of which the Cox-de-Boor algorithm [19] is most popular. This algorithm was also used in this work.

NURBS basis functions (as well as B-spline basis functions) possess some properties that are favorable for their implementation into analysis models. The basis functions possess the local support property, meaning that in every knot span $[\xi_i, \xi_{i+1})$ at most $p+1$ non-zero basis functions exist, namely $N_{i-p,p}, \ldots, N_{i,p}$.

Furthermore, they are non-negative and form a partition of unity at each parametric location. In the interior of the knot span all derivatives of the non-zero basis functions exist and at a knot itself the functions are $p - r$ times continuously differentiable.

The principle of IGA, as was mentioned before, is to use the NURBS basis functions both for describing the geometry and to approximate the unknowns. For the aerodynamic model the unknowns are the doublet strength, as will be explained in section 2.2, and for the structural model the unknowns are the displacements, as will be explained in section 2.3. The power in this approach lies in the fact that the geometry and its boundary discretization can be completely done in CAD software and this geometry can immediately be analyzed in the IGA analysis software.

Even though the exact geometry is provided by the CAD software, the discretization might not be detailed enough to enable the analysis to provide accurate results. This problem can be easily solved by either knot refinement or degree elevation, or a combination of both [20]. The computational algorithms to perform such operations on NURBS functions are well documented in literature [19]. The knot refinement and degree elevation operations have no effect on the geometry itself, making these operations efficient and simple.

2.2. Aerodynamic model

The aerodynamic model is based on the potential flow model, which is characterized by Laplace's equation:

$$\nabla^2 \Phi^* = 0 \tag{5}$$

where Φ^* is the total velocity potential. The boundary conditions for the flow over an airfoil are the flow tangency condition at the boundary of the airfoil and that the disturbance of the flow should go to zero far away from the airfoil:

$$\frac{\partial \Phi^*(\mathbf{x})}{\partial \mathbf{n}} = 0 \text{ for } \mathbf{x} \in \Gamma_b \tag{6}$$

$$\lim_{r \to \infty} \nabla \Phi = 0 \tag{7}$$

where $\mathbf{n}$ is the outward unit normal vector to the boundary of the body Γ_b, r is the distance from the body, and Φ is the perturbation velocity potential. This problem is reduced to solving the following boundary integral equation (BIE) [21]:

$$C(\mathbf{x}_0)\Phi(\mathbf{x}_0) = \int_{\Gamma_b} \left(\frac{\partial \Phi(\mathbf{x})}{\partial \mathbf{n}(\mathbf{x})} G(\mathbf{x}_0, \mathbf{x}) - \Phi(\mathbf{x}) \frac{\partial G(\mathbf{x}_0, \mathbf{x})}{\partial \mathbf{n}(\mathbf{x})} \right) dS(\mathbf{x}) - \int_{\Gamma_w} \Delta\Phi(\mathbf{x}) \frac{\partial G(\mathbf{x}_0, \mathbf{x})}{\partial \mathbf{n}(\mathbf{x})} dS(\mathbf{x}) \tag{8}$$

where $\mathbf{x}_0$ is the point under consideration, $\mathbf{x}$ the point of integration on the surface of the body and the wake, C the jump term, Γ_w the wake surface, and G the fundamental solution as is given in equation 9.

$$G(\mathbf{x}_0, \mathbf{x}) = \frac{1}{2\pi} \log \left(\frac{1}{|\mathbf{x}_0 - \mathbf{x}|} \right) \tag{9}$$

The normal derivative of the fundamental solution is given by

$$\frac{\partial G}{\partial \mathbf{n}}(\mathbf{x}_0, \mathbf{x}) = \frac{(\mathbf{x}_0 - \mathbf{x}) \cdot \mathbf{n}(\mathbf{x})}{2\pi |\mathbf{x}_0 - \mathbf{x}|^2} \tag{10}$$

Setting the normal derivative of the perturbation potential to zero and assuming the notation $C = C(\mathbf{x}_0), \Phi_0 = \Phi(\mathbf{x}_0), \Phi = \Phi(\mathbf{x}), G = G(\mathbf{x}_0, \mathbf{x}), S = S(\mathbf{x}), \mathbf{n} = \mathbf{n}(\mathbf{x})$, gives the following solution:

$$C\Phi_0 = -\int_{\Gamma_b} \Phi \frac{\partial G}{\partial \mathbf{n}} dS - \int_{\Gamma_w} \Delta\Phi \frac{\partial G}{\partial \mathbf{n}} dS \tag{11}$$

When the point $\mathbf{x}_0$ approaches point $\mathbf{x}$ on the boundary of the body, a singularity will be encountered. To desingularize equation 11, the potential inside the body is investigated. The flow tangency boundary condition in equation 6 implies that the potential inside the body is constant. Furthermore, the normal vector is opposite compared to that of the external problem and the jump term becomes $1 - C$ [22]. The following equation thus holds for the interior problem:

$$1 - C = -\int_{\Gamma_b} \frac{\partial G}{\partial \mathbf{n}} dS \tag{12}$$

This relation is fully dependent on the geometry of the problem. Multiplying the equation with the total potential at point $\mathbf{x}_0$ and subtracting it from equation 11 gives

$$\Phi_0 = \int_{\Gamma_b} (\Phi - \Phi_0) \frac{\partial G}{\partial \mathbf{n}} dS \tag{13}$$

which is no longer singular. Combining equation 11 and 13 and introducing the free stream potential Φ_∞, gives the equation for the total velocity potential:

$$\Phi_0^* = -\int_{\Gamma_b} (\Phi - \Phi_0) \frac{\partial G}{\partial \mathbf{n}} dS - \int_{\Gamma_w} \Delta\Phi \frac{\partial G}{\partial \mathbf{n}} dS + \Phi_\infty \tag{14}$$

For the internal problem, the constant velocity potential is set to zero, which results in the final form of the problem that needs to be solved to find the velocity potential along the boundary:

$$-\int_{\Gamma_b} (\Phi - \Phi_0) \frac{\partial G}{\partial \mathbf{n}} dS - \int_{\Gamma_w} \Delta\Phi \frac{\partial G}{\partial \mathbf{n}} dS + \Phi_\infty = 0 \tag{15}$$

The velocity potential jump in the wake is related to the unknown velocity potential distribution on the body through the Kutta condition [23].

The geometry is now discretized using a NURBS curve and the unknown doublet strength is approximated using the same basis functions.

$$\mathbf{x}(\xi) = \sum_{i=1}^{n} R_{i,p}(\xi)\mathbf{P}_i; \quad \Phi(\xi) \approx \sum_{i=1}^{n} R_{i,p}(\xi)\Phi_i \tag{16}$$

Using the dot to indicate derivatives with respect to ξ to simplify notation, the Jacobian of the transformation from the Cartesian coordinate system to the parametric space becomes

$$J(\xi) = \sqrt{\dot{x}_1^2 + \dot{x}_2^2} \tag{17}$$

The non-zero knot spans in the knot vector of the curve can be considered as the elements that build up the geometry. The collocation method is used to set up a linear system of n equations for the $n + 1$ unknown velocity potentials. The final equation is provided by the Kutta condition. The resulting system is as follows:

$$\begin{bmatrix} A_{1,1} & \cdots & A_{1,n} & A_{1,n+1} \\ \vdots & \ddots & \vdots & \vdots \\ A_{n,1} & \cdots & A_{n,n} & A_{n,n+1} \\ -1 & 0 & 1 & -1 \end{bmatrix} \begin{bmatrix} \Phi_1 \\ \vdots \\ \Phi_n \\ \Delta\Phi \end{bmatrix} = \begin{bmatrix} \Phi_\infty^1 \\ \vdots \\ \Phi_\infty^n \\ 0 \end{bmatrix} \tag{18}$$

where $A_{i,j}$ are the aerodynamic influence coefficients. The wake is modeled as a single element with a constant value, so its influence can be computed analytically. The other, non-singular, influence coefficients

are computed numerically in the parametric domain. The integrals, as given in equation 19, are computed using standard Gaussian quadrature. An adaptive scheme is used for the number of integration points to ensure accurate values for near-singular integrals. The number of integration points is increased as a collocation point is closer to the element over which the integral has to be computed.

$$A_{i,j} = \int_0^1 R_{j,p}(\xi) \frac{\partial G(\xi_i, \xi)}{\partial \mathbf{n}} J(\xi) d\xi \tag{19}$$

The desingularized contributions are computed by summing up the non-singular contributions and multiply it with the basis function values in the collocation point.

To find the pressure distribution over the airfoil the flow velocity tangential to the airfoil boundary has to be found. This is found by taking the derivative of the doublet strength in the tangential direction. In conventional panel methods the derivative has to approximated using a finite difference scheme, but since the NURBS curve representing the doublet strength is easily differentiable this can be done exactly:

$$Q_t = \frac{d\Phi}{ds} = \frac{1}{J} \frac{d\Phi}{d\xi} \tag{20}$$

The pressure distribution is now found using equation 21

$$p = -\frac{\rho}{2} \left(Q_t^2 - Q_\infty^2 \right) \tag{21}$$

where p is the pressure, Q_t the tangential velocity, and Q_∞ the free stream velocity. To find the force acting in the control points of the aerodynamic mesh, the pressure is integrated over the element e after multiplication with the corresponding non-zero basis functions in the set $\chi^{(e)}$:

$$\mathbf{f}_n^{\chi(e)} = \int_{\Gamma_e} p(\xi) \mathbf{R}_{\chi(e),p}(\xi) J(\xi) d\xi \tag{22}$$

The aerodynamic model is verified by comparing the results to those obtained using XFOIL [24]. XFOIL is also based on potential flow theory, but uses the traditional discretization into linear panels. When using the inviscid solver within XFOIL, the same results as the model described before should be found. Figure 2 shows the pressure distribution obtained using the present model and XFOIL for a NURBS approximation of the NACA2412 airfoil at an angle of attack of 3 degrees. The control points and weights for the coarse mesh of the airfoil can be found in Appendix A. A good match is observed between the two distributions over the entire chord length. The lift coefficient of the same airfoil for an angle of attack ranging from -8 to 8 degrees is compared in Figure 3. Again a good match is found. Comparison to the experimental results from Abbot and Doenhoff (1959) [25] shows that the inviscid results from both the present model and XFOIL have a slightly higher slope.

2.3. Structural model

The structural model is based on linear curved Timoshenko beams using an isogeometric formulation. Existing work in this field makes use of the local Frenet coordinate system to formulate the beam model [26, 27]. In the present framework, however, a global coordinate system was required to enable the transfer of loads from the aerodynamic model to the structural model and the displacements the other way around. For clarity first the formulation in the Frenet coordinate system is described, followed by the derivation of the formulation in the global coordinate system.

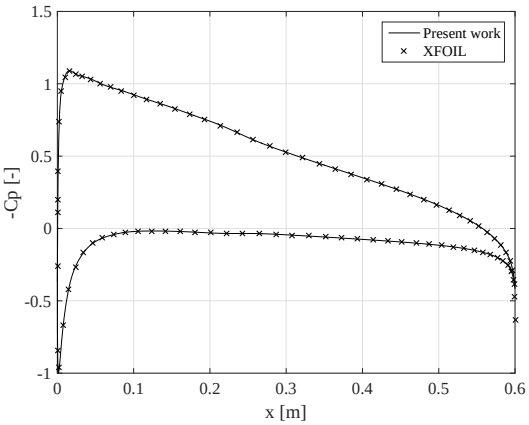

Figure 2: Comparison of results of the present aerodynamic model and XFOIL for the pressure distribution on a NACA 2412 airfoil at an angle of attack of 3 degrees

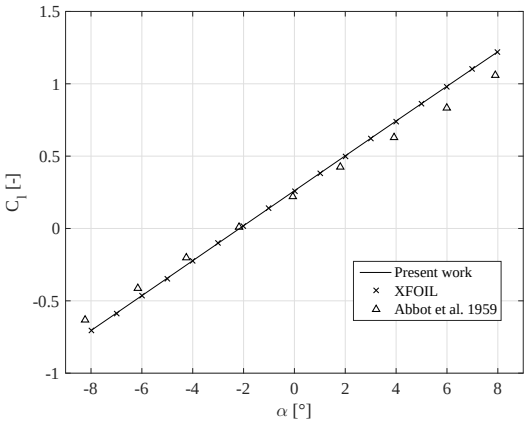

Figure 3: Comparison of results of the present aerodynamic model, XFOIL and experimental data for the lift coefficient of a NACA 2412 at various angles of attack

2.3.1. Local formulation

In the Frenet coordinate system, defined by the tangential, normal and bi-normal unit vectors $(\mathbf{t}, \mathbf{n}, \mathbf{b})$, the membrane, transverse shear and bending strain components of a planar curved beam are defined as

$$\varepsilon_m(s) = \frac{du_t(s)}{ds} - \frac{u_n(s)}{R(s)} \tag{23}$$

$$\gamma_s(s) = \frac{u_t(s)}{R(s)} + \frac{du_n(s)}{ds} - \theta_b(s) \tag{24}$$

$$\chi_b(s) = \frac{d\theta_b(s)}{ds} \tag{25}$$

where u_t, u_n and θ_b are the mid line tangential and normal displacements, and the cross-section rotation, respectively. They are all expressed in the curvilinear coordinate s, as shown in Figure 2.

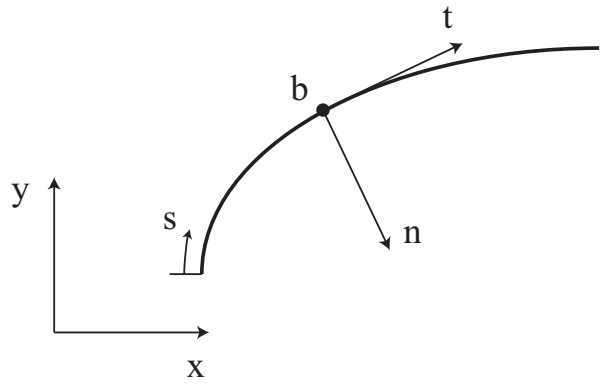

Figure 4: Curved beam coordinate systems

The total potential energy of the planar Timoshenko beam is the sum of the elastic strain energy U, and the potential energy of applied external forces V:

$$\Pi = U + V \tag{26}$$

$$U = \frac{1}{2}\int_0^L \left(EA{\varepsilon_m}^2 + GA\gamma_s^2 + EI\theta_b^2\right)ds \tag{27}$$

$$V = -\int_0^L (\mathbf{f}\cdot\mathbf{u})ds - \mathbf{F}\cdot\mathbf{u} \tag{28}$$

where E and G are the Youngs modulus and shear modulus respectively, A is the cross-sectional area and I is the moment of inertia along $\mathbf{b}$. The vectors $\mathbf{F}$, $\mathbf{f}$ and $\mathbf{u}$ are the concentrated loads, distributed loads, and displacements and rotations, respectively.

The IGA implementation starts with the representation of the geometry using NURBS curves. For simplicity the explanation will first be given for a geometry built up out of a single NURBS curve (single patch). The required modifications for a multi-patch geometry will be described later. The geometry is described by equation 29, where the control points P_i contain the x and y coordinates.

$$\mathbf{x}(\xi) = \sum_{i=1}^{n} R_{i,p}(\xi)\mathbf{P}_i \tag{29}$$

Using the dot to indicate derivatives with respect to ξ to simplify notation, the Jacobian of the transformation from the Cartesian coordinate system to the parametric space becomes

$$J(\xi) = \sqrt{\dot{x}_1^2 + \dot{x}_2^2} \tag{30}$$

and the radius of the beam

$$R(\xi) = \frac{J^3}{|\dot{x}_1\ddot{x}_2 - \ddot{x}_1\dot{x}_2|} \tag{31}$$

The unknown displacements and rotations are approximated using the same basis functions as those that are used to describe the geometry:

$$u_t(\xi) \approx \sum_{i=1}^{n} R_{i,p}(\xi)u_t^i; \quad u_n(\xi) \approx \sum_{i=1}^{n} R_{i,p}(\xi)u_n^i; \quad \theta_b(\xi) \approx \sum_{i=1}^{n} R_{i,p}(\xi)\theta_b^i \tag{32}$$

In the parametric space the strains now become

$$\varepsilon_m(\xi) = \frac{\dot{u}_t}{J} - \frac{u_n}{R} \tag{33}$$

$$\gamma_s(\xi) = \frac{u_t}{R} + \frac{\dot{u}_n}{J} - \theta_b \tag{34}$$

$$\chi_b(\xi) = \frac{\dot{\theta}_b}{J} \tag{35}$$

Substituting equations 32 to 35 in total potential energy equation and taking the second derivative of the strain energy U and the first derivative of the potential energy V with respect to the displacement and rotation control points, will result in the stiffness matrix, $\mathbf{K}$, and force vector, $\mathbf{f}$, respectively. The integrals are computed using Gaussian quadrature at the knot span level. The unknown displacements and rotations, $\mathbf{u}$, are found by simply solving $\mathbf{Ku} = \mathbf{f}$ and substituting the control point values in equation 32.

When the geometry is more complex and cannot be described by a single NURBS patch, multiple patches have to be created and connected to each other. All the patches are interpolatory at the start and end of the curve, simplifying the process of connecting them. In the present work a master-slave technique is used to make sure the patches are connected properly and the redundant slave degrees of freedom are eliminated. The approach also allows connecting patches through hinges by only matching the displacement degrees of

freedom between two patches and leaving the rotation degree of freedom as it is.

2.3.2. Global formulation

To obtain a structural model in a global frame of reference some straightforward changes have to be made to the model described in the previous section. The tangential and normal displacements from the local coordinate system are expressed in the global x and y displacements:

$$u_t(\xi) = \mathbf{u}_g(\xi) \cdot \mathbf{t}(\xi); \quad u_n(\xi) = \mathbf{u}_g(\xi) \cdot \mathbf{n}(\xi) \tag{36}$$

where $\mathbf{u}_g$ is a vector with x and y displacements u and w, and $\mathbf{t}$ and $\mathbf{n}$ are the local tangential and normal vectors, respectively. These unit vectors are derived from the NURBS curve describing the geometry:

$$\mathbf{t} = \begin{bmatrix} \frac{\dot{x}_1}{J} \\ \frac{\dot{x}_2}{J} \end{bmatrix}; \quad \mathbf{n} = \begin{bmatrix} -t_2 \\ t_1 \end{bmatrix} \tag{37}$$

Substituting equation 36 into the strain equations 33 to 35, results in the strains in a global coordinate system:

$$\varepsilon_m(\xi) = \frac{\dot{\mathbf{u}}_g \cdot \mathbf{t} + \mathbf{u}_g \cdot \dot{\mathbf{t}}}{J} - \frac{\mathbf{u}_g \cdot \mathbf{n}}{R} \tag{38}$$

$$\gamma_s(\xi) = \frac{\mathbf{u}_g \cdot \mathbf{t}}{R} + \frac{\dot{\mathbf{u}}_g \cdot \mathbf{n} + \mathbf{u}_g \cdot \dot{\mathbf{n}}}{J} - \theta_b \tag{39}$$

$$\chi_b(\xi) = \frac{\dot{\theta}_b}{J} \tag{40}$$

The derivatives of the unit tangent and normal vectors are equal to

$$\dot{\mathbf{t}} = \begin{bmatrix} \frac{\ddot{x}_1}{J} - \frac{\dot{x}_1 \dot{J}}{J^2} \\ \frac{\ddot{x}_2}{J} - \frac{\dot{x}_2 \dot{J}}{J^2} \end{bmatrix}; \quad \dot{\mathbf{n}} = \begin{bmatrix} -\dot{t}_2 \\ \dot{t}_1 \end{bmatrix} \tag{41}$$

where the derivative of the Jacobian can be found with equation 42:

$$\dot{J} = \frac{\dot{x}_1 \ddot{x}_2 + \ddot{x}_1 \dot{x}_2}{J} \tag{42}$$

The global displacements are again approximated by the NURBS basis functions:

$$u(\xi) \approx \sum_{i=1}^{n} R_{i,p}(\xi) u^i; \quad w(\xi) \approx \sum_{i=1}^{n} R_{i,p}(\xi) w^i \tag{43}$$

The stiffness matrix and force vector in the global coordinate system can now be found by taking the second derivative with respect to the displacements and rotations of the strain energy and the first derivative with respect to the displacements and rotations of the potential energy of the externally applied forces.

Verification of the structural model is performed by comparing its results to some analytical solutions obtained by Cazzani et al. (2014) [27]. The single patch implementation is tested using the vertically loaded cantilever arch shown in Figure 5. The radius R is 2 m, the Young's modulus is 80 GPa, and the Poisson's ratio is 0.2. The cross-section of the arch is rectangular with the thickness h equal to 0.01 m and the depth equal to 0.2 m. A vertical unit load P is applied at the tip of the arch. The vertical displacement at the tip of the arch is computed using the described structural model for an increasing number of elements. The convergence plot in Figure 6 shows that the displacement converges nicely to the analytical value.

The multi-patch implementation of the structural model is verified using the vertically loaded incomplete ring shown in Figure 7. The single patch making up the geometry is split at point A to create two separate patches. The radius R is 2.935", the Young's modulus $1.05 \cdot 10^7$ psi, and the Poisson's ratio 0.3. The cross-section of the beam is rectangular with a thickness h of 0.125" and a depth of 1.2". The vertical displacement

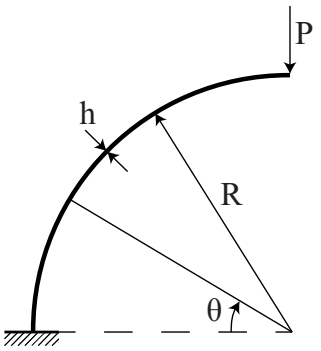

Figure 5: Sketch of the vertically loaded cantilever arch

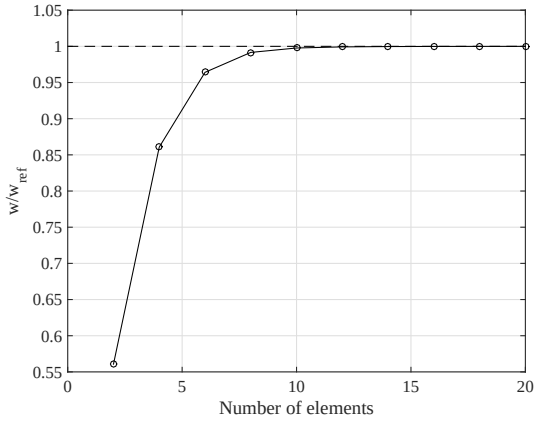

Figure 6: Convergence plot for the single patch cantilever arch

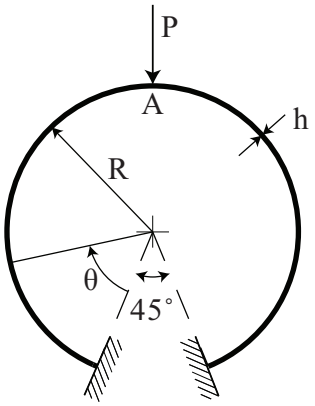

Figure 7: Sketch of the vertically loaded incomplete ring

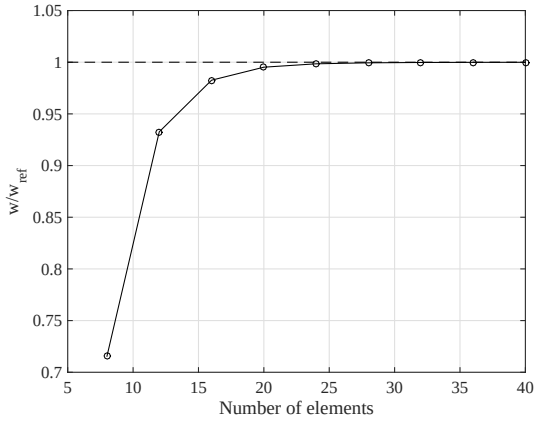

Figure 8: Convergence plot for the multi-patch incomplete ring

in point A is computed for an increasing number of elements and the convergence plot is shown in Figure 8. Again a nice convergence towards the analytical result is observed.

2.4. Coupling

The aerodynamic and structural models are closely coupled, to enable fast computation of the converged solution. The coupling scheme is based on the conservation of energy, meaning that the virtual work, δW, done by the aerodynamic loads on the aerodynamic mesh should be equal to the work done by the equivalent set of loads on the structural mesh [28]:

$$\delta W = \delta \mathbf{u}^T \cdot \mathbf{f}_{aero} = \delta \mathbf{u}_a^T \cdot \mathbf{f}_{aero}^a \tag{44}$$

where $\delta \mathbf{u}$ and $\delta \mathbf{u}_a$ are the virtual displacements of the structural and aerodynamic control points and $\mathbf{f}_{aero}$ and $\mathbf{f}_{aero}^a$ are the aerodynamic forces acting on the structural and aerodynamic control points. To achieve a close coupling, a coupling matrix $\mathbf{H}$ is required which couples the aerodynamic displacements to the structural displacements:

$$\mathbf{u}_a = \mathbf{H} \cdot \mathbf{u} \tag{45}$$

Inserting equation 45 into equation 44 shows that in that case the following relation also holds:

$$\mathbf{f}_{aero} = \mathbf{H}^T \cdot \mathbf{f}_{aero}^a \tag{46}$$

Conventional methods for finding this coupling matrix, such as radial basis function interpolation, fail in the current work due to the fact that the control points of the IGA mesh are not always located on the boundary. In the present work both the structural mesh and aerodynamic mesh originate from a coarse initial mesh, as is illustrated in Figures 9 to 11.

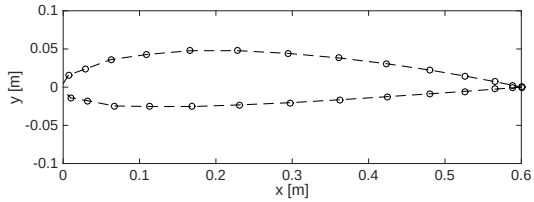

Figure 9: Example of a coarse control polygon

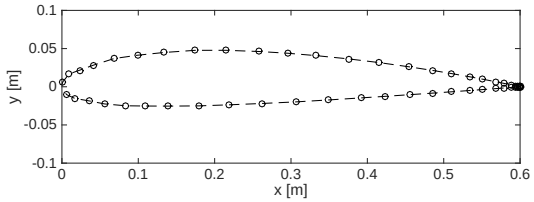

Figure 10: Aerodynamic mesh derived from the control polygon in Figure 9

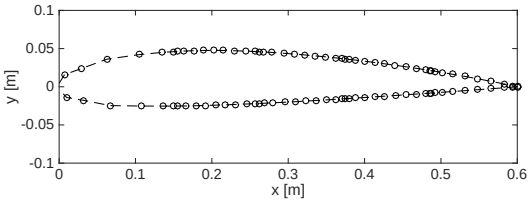

Figure 11: Structural mesh derived from the control polygon in Figure 9

To obtain the required coupling matrix the sensitivity matrices for the structural and aerodynamic mesh with respect to the coarse mesh are used. These sensitivity matrices describe how the control points in either the aerodynamic or structural mesh move as the control points in the coarse mesh are moved and can thus be used to link the aerodynamic displacements, $\mathbf{u}_a$, to the structural displacements, $\mathbf{u}$:

$$\mathbf{u}_a = \mathbf{H} \cdot \mathbf{u} = \frac{d\mathbf{P}_{aero}}{d\mathbf{P}_{struct}} \cdot \mathbf{u} = \frac{d\mathbf{P}_{aero}}{d\mathbf{P}_{coarse}} \cdot \left(\frac{d\mathbf{P}_{struct}}{d\mathbf{P}_{coarse}} \right)^{-1} \cdot \mathbf{u} \tag{47}$$

Both the aerodynamic and structural model are linear, so a single Newton-Raphson iteration gives the converged displacement field:

$$\begin{aligned}(\mathbf{K}_s - \mathbf{K}_a^s) \cdot \mathbf{u} &= \mathbf{f}_{aero,0}^s + \mathbf{f}_0 \\ \mathbf{K}_a^s &= \mathbf{H}^T \cdot \mathbf{K}_a \cdot \mathbf{H} \\ \mathbf{f}_{aero,0}^s &= \mathbf{H}^T \cdot \mathbf{f}_{aero,0}\end{aligned} \tag{48}$$

where $\mathbf{K}$ are the stiffness matrices and $\mathbf{f}_0$ any external force besides the aerodynamic load. The superscript s indicates that the values are in terms of the structural degrees of freedom and the subscript 0 indicates that the forces are those acting on the undeformed geometry. The converged aerodynamic forces are computed using the displacement field obtained by solving equation 48:

$$\mathbf{f}_{aero} = \mathbf{f}_{aero,0} + \mathbf{K}_a \cdot \mathbf{H} \cdot \mathbf{u} \tag{49}$$

From these converged aerodynamic forces the lift coefficient can be determined, by taking into account the angle of attack.

2.5. Boundary layer model

To gain some insight in the viscous effects, such as drag and flow separation, a boundary layer model is coupled to the aeroelastic model described in the previous subsections. The input into this boundary layer model is the deformed geometry obtained from the aeroelastic analysis. A flow-chart of the system is given in Figure 12.

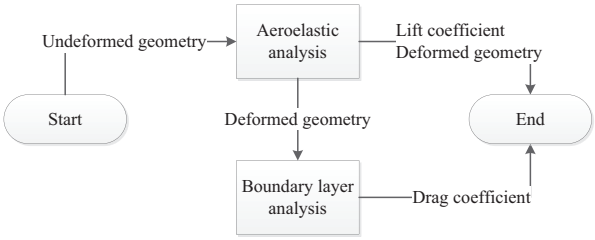

Figure 12: Flowchart of the analysis module

The deformed geometry is used to obtain the tangential velocity distribution along the boundary of the airfoil. Using a boundary layer model based on the one described by Moran [29], which is based upon several semi-empirical methods, the growth of the boundary layer along the airfoil is computed. The laminar part of the boundary layer is described by Thwaites' method and the turbulent part by Head's method. The transition between the two different flow states is determined using Michel's method. The tangential velocity distribution is discretized into small elements along the boundary and using these methods the development of the boundary layer is computed step-by-step from the front stagnation point to the trailing edge.

The main modifications compared to the original implementation are made in the transition and separation steps. To be able to use the drag coefficient in a gradient-based optimization process the response surface should be continuous. Therefore, instead of only determining the element in which transition or separation occurs and assuming that the full element is turbulent or separated, an interpolation is done to find the location of transition or separation more accurately. This prevents any jumps in the response when the location switches from one element to the next.

The profile drag coefficient is subsequently determined using the Squire-Young formula, which takes into account the momentum thickness and displacement thickness at the upper and lower side of the trailing edge of the airfoil [30].

For verification of the boundary layer model, its results are compared to those obtained using XFOIL. The drag coefficient of a NACA2412 airfoil at an angle of attack ranging from 0 to 10 degrees at a Reynolds number of one million is computed using the presented boundary layer model and XFOIL. The results are shown in Figure 13. For this range of interest the results match quite well, especially when realizing that

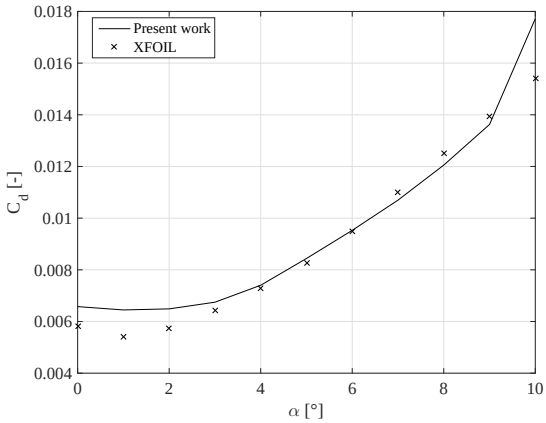

Figure 13: Comparison of results of the present boundary layer model and XFOIL for the drag coefficient of a NACA2412 airfoil for different angles of attack at a Reynolds number of one million

whereas XFOIL makes use of a two-way coupling of the aerodynamic and boundary layer model and a more sophisticated drag prediction, the present framework only uses a one-way coupling in combination with the Squire-Young formula. The deviation at higher angles of attack is probably caused by flow separation, as the results from the Squire-Young formula become inaccurate as soon as separation takes place. Most important is that the trend matches the XFOIL results, making the present implementation suitable for optimization.

3. Morphing airfoil optimization

The aeroelastic framework described in the previous section is applied to the optimization of an active morphing airfoil. The goal is to morph the baseline airfoil shape, designed for optimal performance during cruise flight, into an airfoil shape more suitable for landing conditions. This means that the lift coefficient of the airfoil at a certain angle of attack needs to be maximized resulting in a reduced minimum landing speed and thus increased landing performance. In section 3.1, a description is given for the design case, including the unmanned aerial vehicle (UAV) under consideration and the flight conditions of interest to the optimization problem. Section 3.2 covers the setup of the optimization problem. The objective, constraints and design variables will be presented.

3.1. Design case

The UAV considered for the optimization has a mass of 25 kg and its wings are rectangular with the NACA2412 airfoil. The wingspan is 3.0 m and the chord length is 0.6 m. The cruise and landing flight conditions are listed in Table 1.

Table 1: Flight conditions for UAV in cruise and landing flight

		Cruise	Landing
Speed	[km/h]	110	56.02
Altitude	[m]	304.8	304.8
Angle of attack	[deg]	-	6.373
Lift coefficient	[-]	0.2425	-

The internal structure of the airfoil consists of a stiff wing box in the leading edge, with a single spar at 25.00% of the chord. The actuators are located at 43.75%, 62.50% and 81.25% of the chord and have a vertical orientation in the undeformed NACA2412 airfoil. The actuators are connected to the skin through hinges. Throughout all the analyses and optimization runs the front spar of the airfoil is fully clamped. An illustration of the structure is shown in Figure 14.

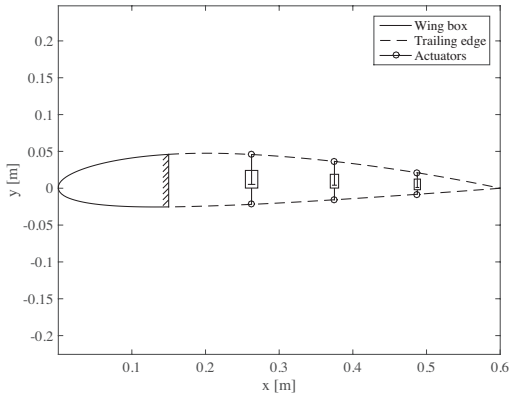

Figure 14: Geometry and internal structure of the morphing airfoil

3.2. Optimization setup

The main objective of the optimization is to maximize the lift coefficient in landing flight conditions, while the NACA2412 geometry is maintained during other flight conditions. Without taking into account viscous effect, however, this would lead to infeasible results where flow separation would cause bad performance in landing conditions. The viscous effects are introduced into the optimization by including the drag coefficient into the objective function. Instead of simply optimizing the lift coefficient, the ratio of the lift and drag coefficient is optimized. The emphasis is put on the lift coefficient by raising it to a certain power. In the present work a power of 1.5 is used, which leads to realistic results where the influence of the lift coefficient is still dominating. This approach requires a two-step optimization to avoid conservative results due to local minima present in the objective function, as is demonstrated in the next section.

Two separate analysis runs are done. One at landing conditions with the actuators enabled and one at 2.5g flight conditions with the actuators locked. Additional constraints are added to ensure a feasible design is found:

- Strain constraints are used for the airfoil skin in the morphing section. The IGA framework allows easy strain evaluations at any point on the geometry. In the present work the strain at 100 evenly spaced points were taken into account as constraints. The maximum allowed strain is 4000 microstrain.
- Constraints on the maximum actuation forces and maximum actuator strokes are implemented to avoid infeasible actuator requirements. The maximum value for the actuation force is set to 500N and the actuator stroke may be at most 40% of the initial length.
- When lamination parameters are included as design variables a set of constraint equations is implemented to ensure feasible laminate designs.

Besides the lamination parameters, the thickness and actuation forces are also included as design variables. The lamination parameters, however, deviate from the standard lamination parameters, because the current framework only covers two-dimensional problems. A modified set of lamination parameters is used to scale the membrane and bending stiffness of the laminate [31]:

$$EI = \alpha \frac{wh^3 E_{ref}}{12} \tag{50}$$

$$EA = \beta whE_{ref} \tag{51}$$

where h and w are the thickness and width of the laminate, and E_{ref} is the reference Young's modulus of the material. In the current work the modulus in the fiber direction of the material used in the optimization,

carbon fiber AS4/8773, was selected as the reference Young's modulus. The specifications of the material are given in Table 2.

Table 2: Material properties of carbon fiber AS4/8773

		AS4/8773
E_1	$[N/m^2]$	1.198×10^{11}
E_2	$[N/m^2]$	9.08×10^9
G_{12}	$[N/m^2]$	5.29×10^9
ν	[-]	0.32
t_{ply}	$[m]$	1.83×10^{-4}

A set of boundaries for the feasible design space was found by simply checking many different laminates and take the outer boundaries of the dataset. For unidirectional pre-impregnated carbon fiber in an epoxy material AS4/8773 the bounding box is created by the following equations:

$$\begin{aligned} -\beta_i + 0.474\alpha_i + 0.0368 \leq 0, &\quad \text{for } i = 1 \dots N_p \\ \beta_i - 1.3013\alpha_i + 0.5656 \leq 0, &\quad \text{for } i = 1 \dots N_p \\ \beta_i - 9.4808\alpha_i + 8.8408 \leq 0, &\quad \text{for } i = 1 \dots N_p \\ -\beta_i + 0.4694\alpha_i + 0.5306 \leq 0, &\quad \text{for } i = 1 \dots N_p \\ -\beta_i + 1.2842\alpha_i + 0.2476 \leq 0, &\quad \text{for } i = 1 \dots N_p \\ \beta_i - 8.9981\alpha_i + 0.5595 \leq 0, &\quad \text{for } i = 1 \dots N_p \end{aligned} \tag{52}$$

The design space of a laminate with fewer layers is conservative with respect to the design spaces of a laminate with more layers, so a minimum thickness can be chosen and the design space for this thickness can be safely used for thicker lamina as well.

The globally convergent method of moving asymptotes (GCMMA) [32] is used to perform the gradient-based optimization. The objective, constraints and design variables are all normalized or scaled such that their magnitudes are similar. The direct sensitivities are computed using algorithmic differentiation in all three models, ensuring efficient computation and accurate sensitivities [33]. The Karush-Kuhn-Tucker optimality conditions are used as convergence criterion.

Four different optimization cases are studied in the present work.

- First of all, a baseline optimization is done where only the actuation forces are included as design variables. The thickness for the baseline is chosen such that the cruise geometry can still be closely maintained during the 2.5g load case and is equal to 20 plies, or 3.66 mm. The laminate is set to a quasi-isotropic one by setting the lamination parameters to 0.5.
- The second optimization also includes the thickness of the skin as design variable besides the actuation forces.
- The third case uses the actuation forces and lamination parameters to obtain an optimal result.
- The final optimization includes all the design variables and should theoretically give the best result.

Table 3 gives and overview of the settings per optimization case.

4. Results

As was mentioned in the previous section, the drag coefficient was included in the objective function to ensure a feasible result without flow separation. To show the influence of the objective function formulation on the final morphed airfoil, both single step and double step optimization approaches will be discussed. In the first subsection the single step optimization approaches, using the inverse of the lift coefficient or the

Table 3: Settings for the four optimization cases

#		Skin thickness	Actuation forces	Lamination parameters
1	Baseline	3.66 mm	Free	a = b = 0.5
2	Thickness	Free	Free	a = b = 0.5
3	Laminate	3.66 mm	Free	Free
4	Thickness + laminate	Free	Free	Free

fraction of drag and lift coefficient as objective function, are presented . Subsequently, the final two-step optimization formulation result is shown and the results for the four optimization cases are presented and discussed.

4.1. Single step optimization

The single step optimization approaches are only demonstrated for the fourth optimization case, which includes both thickness and lamination parameters as design variables. The effect of the objective function will be most pronounced for this case. The results from the optimization based on only the lift coefficient is presented first. Subsequently, the results from the optimization using both drag and lift coefficient are presented.

4.1.1. $1/C_l$ *minimization*

In Figure 15 the deformed airfoil is shown. At the trailing edge a large deformation can be seen. This deformation causes the flow to separate, which is unfavorable during any flight condition. The lift coefficient

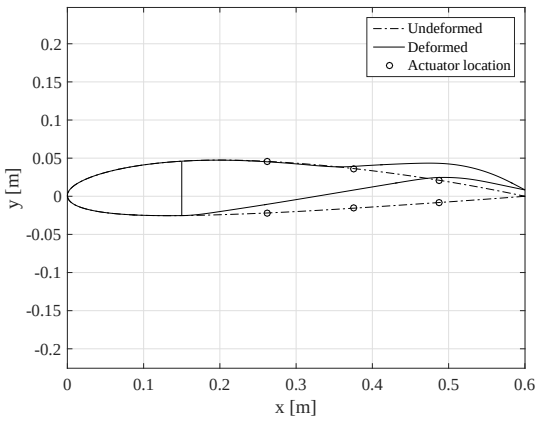

Figure 15: Deformed airfoil for lift coefficient maximization for optimization case 4

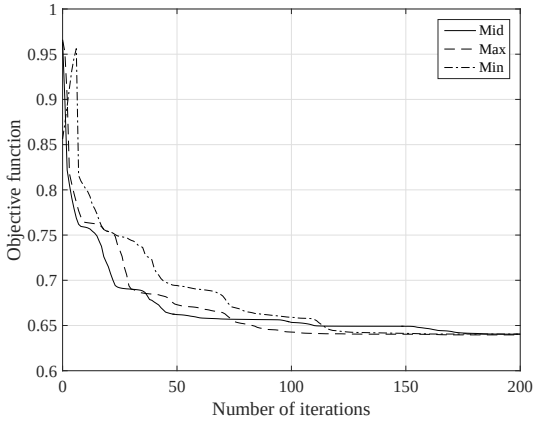

Figure 16: Objective function optimization history for three different initial design variable sets for optimization case 4

for the deformed airfoil is 1.56 and the drag coefficient is equal to 0.0181.

The solution of this optimization approach is insensitive with respect to the initial design vector. In Figure 16 the optimization history of the objective function is shown for three different starting points. The solid line represents the starting point as mentioned in the previous section, with the design variables in the middle of their ranges. The dashed and dashed-dotted lines result from starting close at the maximum and minimum of the variable ranges, respectively. The figure shows that all optimizations converge to the same objective function value and on inspection of the resulting geometries it can indeed be concluded that the same solution has been found in all three cases.

4.1.2. $C_d/C_l^{1.5}$ minimization

Taking the objective function equal to $C_d/C_l^{1.5}$ results in a much more conservative solution. The increased complexity of the objective functions introduces more local minima, so the chances of the optimizer ending up in one of these minima is increased. The resulting deformation in Figure 17 indeed shows that the deformation is less pronounced compared to Figure 15. A lift coefficient of 1.148 and a drag coefficient

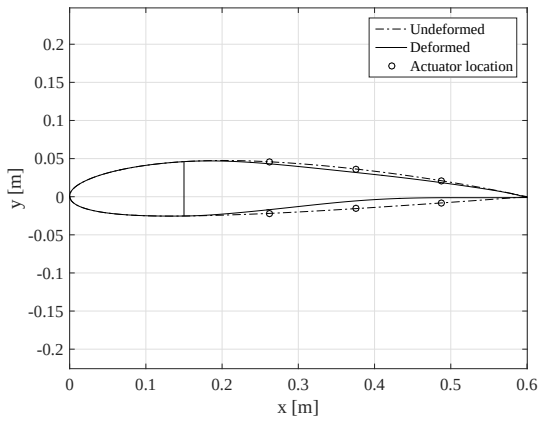

Figure 17: Deformed airfoil for $C_l^{1.5}/Cd$ maximization for optimization case 4

of 0.0106 is found for this airfoil.

4.2. Two-step optimization results

Neither of the morphing airfoils found in the previous two subsections satisfy the requirements. The first airfoil experiences too much deformation, causing flow separation. The second airfoil is still far away from the possible increase in lift as demonstrated by the first airfoil. From these results the idea was formulated to create a hybrid two-step optimization approach. The two steps are as follows:

1. The maximum possible lift coefficient is found by using the inverse of the lift coefficient as objective function.
2. From that point in the design space, the next optimization step is started with the drag coefficient included in the objective function and the lift coefficient raised to the power 1.5.

The benefit of this approach is that it will be insensitive to the initial design vector, as was shown in subsection 4.1.1. The second step is more sensitive to the starting design, but as this point is always the same this is not a problem. The optimizer will thus find a solution close to the solution with the maximum lift coefficient, but a little bit more conservative to avoid flow separation.

This two-step optimization approach is used for the four optimization cases described in previous section. The results are presented in the remainder of this subsection. A summary of the optimization results is given in Table 4. An increase in the lift and drag coefficient is observed for all designs compared to the NACA2412 airfoil. The optimization histories for the objective function in the first and second optimization step are collected in Figures 18 and 19. In the first step the objective function converges faster as less design variables are involved. In the second step only the case with both the thickness and lamination parameters included changes significantly. The other cases were not able to achieve a solution with flow separation in the first optimization step due to the bounds on the design variables. The minimum in the second step thus coincided with that of the first step. The combined effect of the thickness and lamination parameters enables a more extreme deformation and thus results in flow separation and a large increase in drag in the first step.

In the following subsections more details will be given per design. First the baseline result is presented to understand what the performance of a non-optimized structure would be. The results of the other

Table 4: Objective function and lift and drag coefficient for the NACA2412 and the four optimization cases

	Objective function $[\cdot 10^{-3}]$	Lift coefficient [-]	Drag coefficient [-]
NACA2412	10	1.028	0.0105
Baseline	9.58	1.074	0.0107
Thickness	9.54	1.318	0.0144
Laminate	9.46	1.259	0.0134
Thickness + laminate	8.80	1.459	0.0155

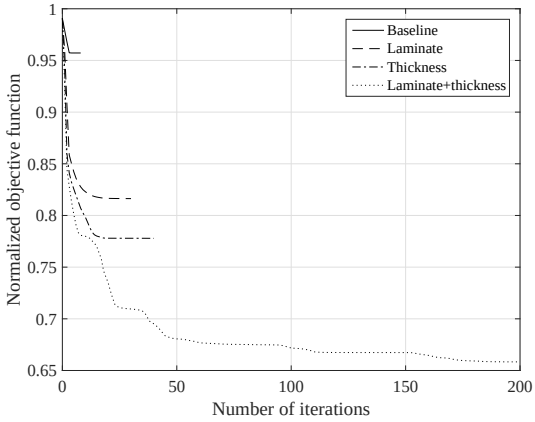

Figure 18: Objective function optimization histories for the first optimization step for the four cases normalized with respect to the undeformed NACA2412 performance

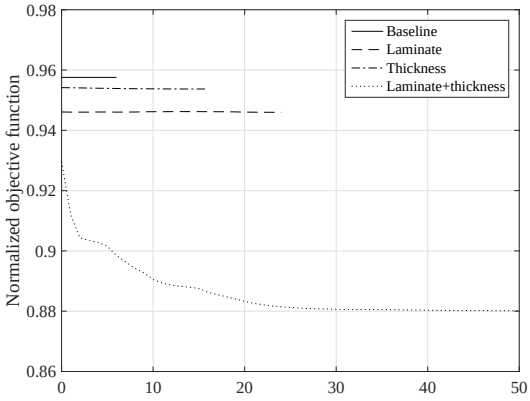

Figure 19: Objective function optimization histories for the second optimization step for the four cases normalized with respect to the undeformed NACA2412 performance

optimization cases are compared with the baseline, but also with each other. Finally, the absence of flow separation is investigated.

4.2.1. Baseline

The undeformed NACA2412 airfoil in landing conditions has a lift coefficient of 1.028 and a drag coefficient of 0.0105, resulting in a value of 0.01 for the objective function. For the baseline configuration only the actuation forces are optimized, as was explained before.

The resulting deformed shape with the constant skin thickness and quasi-isotropic layup is shown in Figure 20, together with the undeformed shape and actuator connection points.

It is visible that the thickness of the trailing edge is decreased and the camber is slightly increased, which indeed results in an increase in lift coefficient. The objective function for the baseline case is equal to $9.58 \cdot 10^{-3}$, which translates into a lift coefficient of 1.074 and a drag coefficient of 0.0107. A slight increase in both lift and drag is thus achieved compared to the NACA2412 airfoil.

Because the thickness and lay-up is uniform throughout the skin, the deformation is almost symmetric. The actuation force in this case limits the deformation. All three actuation force design variables are hitting their upper limit of 500N, preventing the optimizer to move towards more extreme camber lines. None of the other constraints are active. The cruise shape is maintained during the 2.5g load case. The strain in the skin is shown in Figure 21, which shows that it does not reach the limit anywhere. Similar as the deformation, the strain is also nearly symmetric on the upper and lower surface.

4.2.2. Skin thickness optimization

Figure 22 shows the deformed shape resulting from the skin thickness optimization. The actual skin thickness distribution is shown in Figure 23, where also the skin thickness of the baseline structure is shown for comparison. The variation in skin thickness allows the optimizer to introduce more camber compared

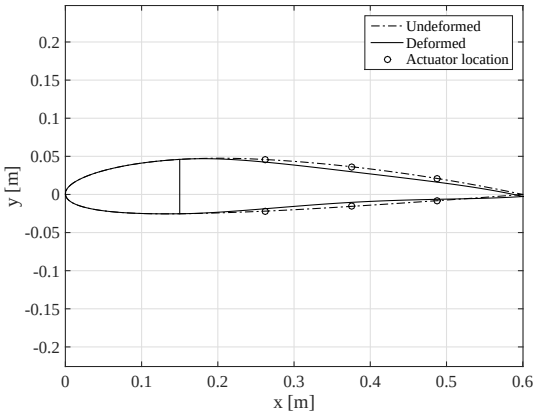

Figure 20: Baseline deformed and undeformed shape in landing flight conditions

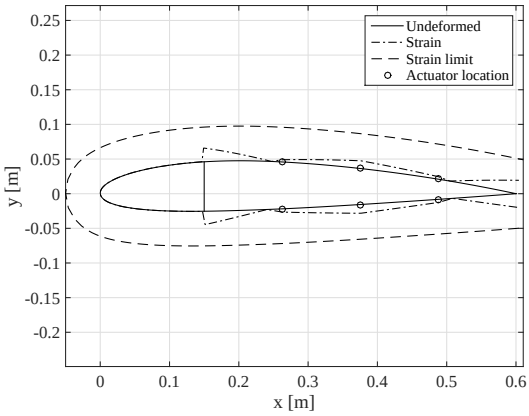

Figure 21: Strain in the skin of the baseline configuration

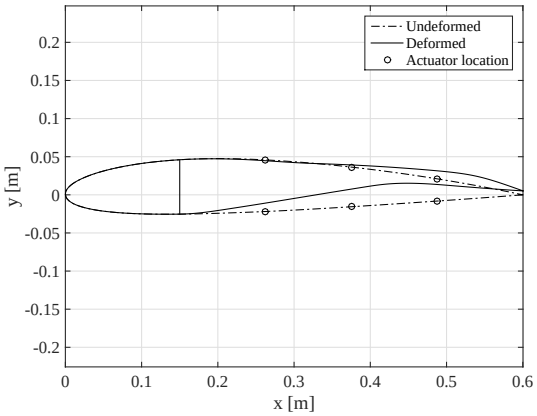

Figure 22: Thickness optimisation resulting deformation

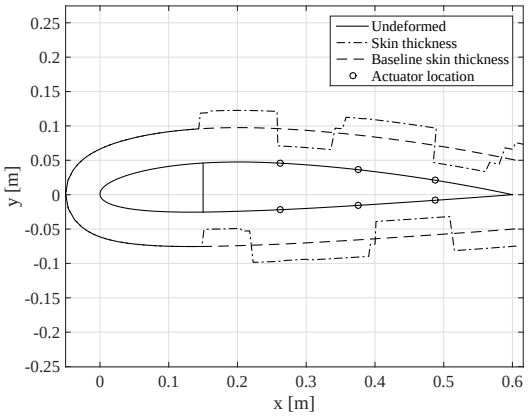

Figure 23: Thickness optimisation resulting thickness distribution

to the baseline result. This results in an increased lift coefficient of 1.318, which is significantly higher than that of the NACA2412 and baseline airfoils.

The thickness distribution shows that most of the thickness design variables are at their limit values. The thickness of the skin connected to the spar at the bottom side has the lowest thickness possible to introduce a compliant hinge. At the top the opposite is observed. The thickness is increased to the maximum value in order to maintain a stiff connection in this location. This allows for more camber to be introduced in the structure.

The middle and last actuators are at their maximum stroke and force, and the strain approaches the strain limit in most of the thin sections, as is shown in Figure 24. The cruise shape is again maintained during the 2.5g load case.

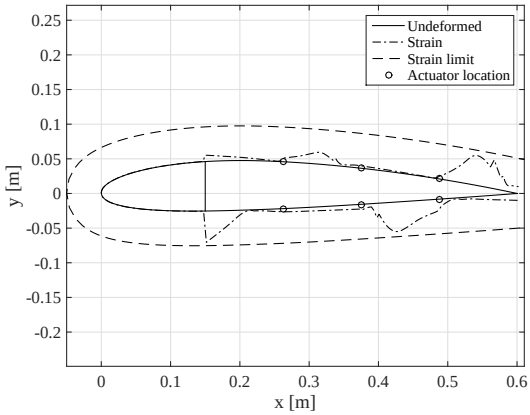

Figure 24: Strain in the skin of the thickness optimized configuration

4.2.3. Laminate optimization

The skin deformation and lamination parameters for the laminate optimization case are shown in Figure 7, and Figures 8 and 9, respectively. The deformation is again larger compared to the baseline, but less severe compared to the thickness optimization case. This is also reflected in the resulting lift coefficient of 1.259, which is in between the baseline and thickness optimization values.

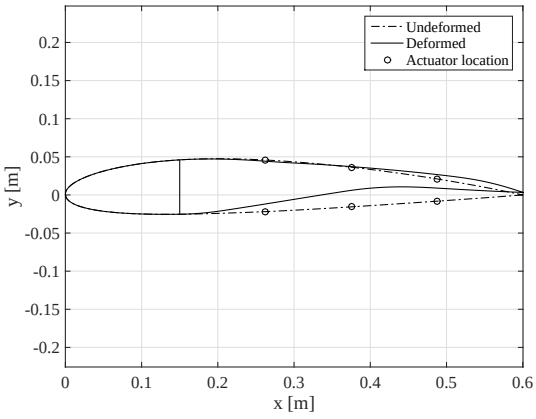

Figure 25: Laminate optimization resulting deformation

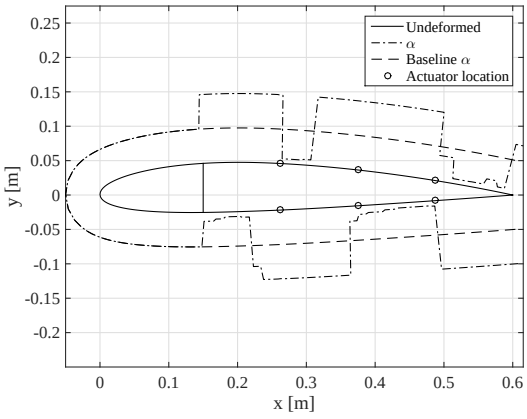

Figure 26: Laminate optimization resulting α distribution

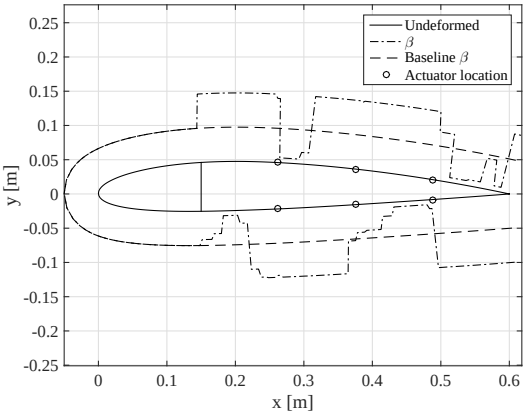

Figure 27: Laminate optimization resulting β distribution

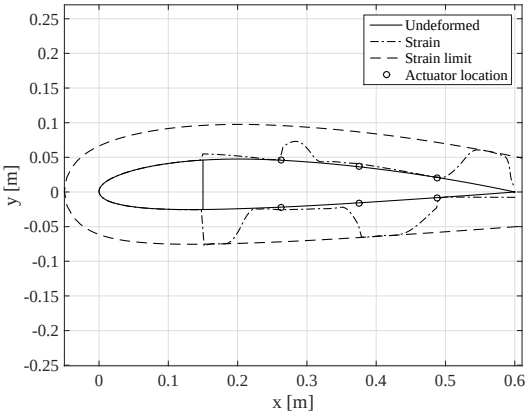

Figure 28: Strain in the skin of the laminate optimized configuration

The lamination parameters both show similar behavior as the thickness distribution in the previous case. The stiffness is strongly reduced and increased in same sections as where the thickness was reduced and increased in the previous results. The thickness, however, has a larger influence on the bending stiffness, explaining the larger displacement for the skin thickness optimization.

Similar as to the previous results, the middle and last actuator reach their maximum stroke and force. Figure 28 shows that the strain limit is now reached in three out of four flexible sections. The cruise shape is maintained during the 2.5g load case.

4.2.4. Skin thickness and laminate optimization

Figures 29 and 30 to 32 show the deformation and design variable distribution for the optimization case with both the thickness and lamination parameters included as variables. The increased design freedom results in the highest lift coefficient of 1.459, achieved by the bigger displacement and larger curvature of the trailing edge compared to the previous results.

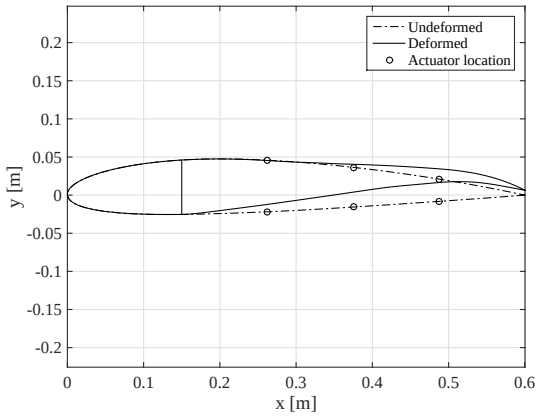

Figure 29: Thickness and laminate optimization resulting deformation

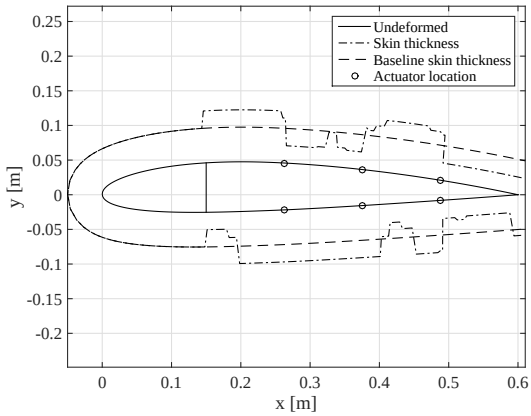

Figure 30: Thickness and laminate optimization resulting thickness distribution

Contrary to the previous results, which showed very similar trends, this design case shows different behavior near the trailing edge. In the previous results both the upper and lower skin at the trailing edge were stiff, but in this case all design variables go the to minimum value on the upper side. When comparing

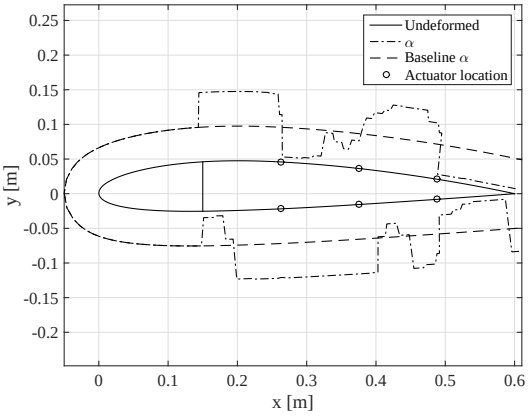

Figure 31: Thickness and laminate optimization resulting α distribution

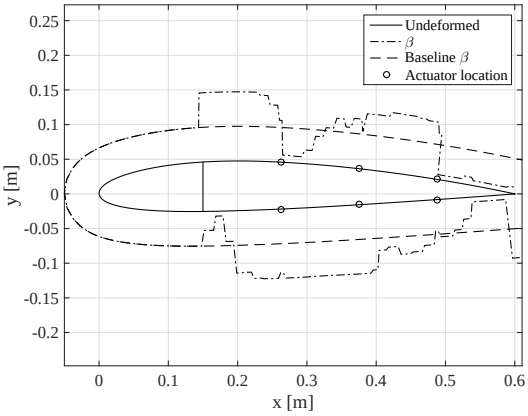

Figure 32: Thickness and laminate optimization resulting β distribution

the design variables within the optimization case, it can be seen that the results are very similar in terms of stiff and compliant sections.

The actuator closest to the trailing edge reaches maximum force and stroke, while the one furthest away from the trailing edge reaches an actuation force of zero. The middle actuator exerts a force of approximately 215N. The strain in the skin close to the trailing edge reaches the limit, as well as the strain at the bottom of the spar. This is illustrated in Figure 33.

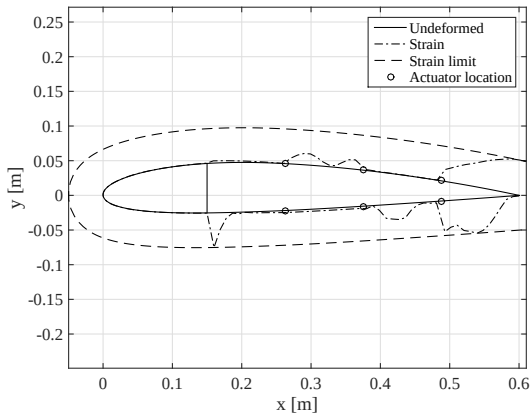

Figure 33: Strain in the skin of the thickness and laminate optimized configuration

4.3. Attached flow

The drag coefficient was added to the objective function to make sure the optimized results would be separation free, as was mentioned before. In Figure 34 the skin friction coefficient on the upper and lower surface of the last airfoil is shown, as computed by XFOIL. The curve for the upper surface clearly shows the transition point at around 14% of the chord, because the friction coefficient rises sharply at that point. On the bottom surface the same phenomenon can be observed at the transition point at around 69% chord. At the trailing edge the friction coefficient on the upper surface decreases towards zero, but is still slightly above. When the friction coefficient is equal to or lower than zero the flow has separated, so this shows that indeed no flow separation is taking place.

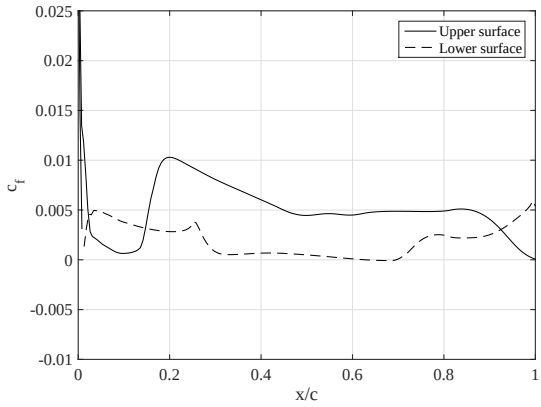

Figure 34: Development of skin friction coefficient in the boundary layer on the upper and lower surface of the airfoil with optimized skin thickness and laminate

5. Conclusions

A two-dimensional low-fidelity isogeometric aeroelastic optimization framework was presented and applied to the optimization of an active morphing airfoil. The framework consists of an isogeometric BEM potential flow solver and an isogeometric curved Timoshenko beam solver, which are closely coupled. The coupling matrix is derived from the sensitivity matrices of the structural and aerodynamic control points with respect to a shared coarse control polygon. Both solvers make use of NURBS basis functions to describe the geometry and approximate the unknown variables. A boundary layer model is included in the framework to enable the computation of viscous effects.

The integrals for the aerodynamic model are desingularized, enabling easy calculation of the originally singular contributions to the aerodynamic influence coefficients. The multi-patch beam model is formulated in a global frame of reference to simplify the coupling to the aerodynamic model. The patches are connected through a master slave technique, enabling both rigid connections and hinged connections. The boundary layer model is based on existing semi-empirical integral methods improved with interpolation techniques to accurately determine points of flow transition or separation.

The aeroelastic optimization framework was used to optimize the landing performance of a 25kg UAV. The airfoil shape for cruise conditions was set to a NACA2412 and the goal was to maximize the lift coefficient during landing flight conditions by adding three actuators in the trailing edge of the airfoil and optimizing the skin thickness and lamination parameters. Four cases were optimized with varying design variables. To ensure feasible results without significant flow separation the drag coefficient was added to the objective function.

The results showed that higher lift coefficients were achieved, as more design variables were included, as was expected. The skin thickness was shown to be the most important design variable in the presented design case, because the structure is predominantly loaded in bending. The inviscid results showed an increase in lift coefficient of up to 42% for the case with both skin thickness and lamination parameter as design variables. Analysis of the airfoil in Xfoil showed that indeed no flow separation was taking place, caused by the use of the drag coefficient in the objective function.

References

[1] T. J. R. Hughes, J. A. Cottrell, Y. Bazilevs, Isogeometric analysis: CAD, finite elements, NURBS, exact geometry and mesh refinement, Computer Methods in Applied Mechanics and Engineering 194 (3941) (2005) 4135–4195. doi:10.1016/j.cma.2004.10.008.

[2] V. P. Nguyen, C. Anitescu, S. P. A. Bordas, T. Rabczuk, Isogeometric analysis: An overview and computer implementation aspects, Mathematics and Computers in Simulation 117 (2015) 89–116. doi:10.1016/j.matcom.2015.05.008.

[3] Y. Bazilevs, M.-C. Hsu, J. Kiendl, R. Wüchner, K.-U. Bletzinger, 3D simulation of wind turbine rotors at full scale. Part II: Fluidstructure interaction modeling with composite blades, International Journal for Numerical Methods in Fluids 65 (1-3) (2011) 236–253. doi:10.1002/fld.2454.
[4] Y. Bazilevs, M. C. Hsu, M. A. Scott, Isogeometric fluid-structure interaction analysis with emphasis on non-matching discretizations, and with application to wind turbines, Computer Methods in Applied Mechanics and Engineering 249252 (2012) 28–41. doi:10.1016/j.cma.2012.03.028.
[5] A. Korobenko, M.-C. Hsu, I. Akkerman, J. Tippmann, Y. Bazilevs, Structural mechanics modeling and FSI simulation of wind turbines, Mathematical Models and Methods in Applied Sciences 23 (02) (2012) 249–272. doi:10.1142/S0218202513400034.
[6] Y. Bazilevs, V. M. Calo, Y. Zhang, T. J. R. Hughes, Isogeometric fluid-structure interaction analysis with applications to arterial blood flow, Computational Mechanics 38 (4-5) (2006) 310–322. doi:10.1007/s00466-006-0084-3.
[7] Y. Bazilevs, J. R. Gohean, T. J. R. Hughes, R. D. Moser, Y. Zhang, Patient-specific isogeometric fluid-structure interaction analysis of thoracic aortic blood flow due to implantation of the Jarvik 2000 left ventricular assist device, Computer Methods in Applied Mechanics and Engineering 198 (4546) (2009) 3534–3550. doi:10.1016/j.cma.2009.04.015.
[8] C. Politis, A. I. Ginnis, P. D. Kaklis, K. Belibassakis, C. Feurer, An isogeometric BEM for exterior potential-flow problems in the plane, in: 2009 SIAM/ACM Joint Conference on Geometric and Physical Modeling, SPM '09, ACM, New York, NY, USA, 2009, pp. 349–354. doi:10.1145/1629255.1629302.
[9] T. Takahashi, T. Matsumoto, An application of fast multipole method to isogeometric boundary element method for Laplace equation in two dimensions, Engineering Analysis with Boundary Elements 36 (12) (2012) 1766–1775. doi:10.1016/j.enganabound.2012.06.004.
[10] L. Heltai, M. Arroyo, A. DeSimone, Nonsingular isogeometric boundary element method for Stokes flows in 3D, Computer Methods in Applied Mechanics and Engineering 268 (2014) 514–539. doi:10.1016/j.cma.2013.09.017.
[11] R. N. Simpson, S. P. A. Bordas, J. Trevelyan, T. Rabczuk, A two-dimensional isogeometric boundary element method for elastostatic analysis, Computer Methods in Applied Mechanics and Engineering 209212 (2012) 87–100. doi:10.1016/j.cma.2011.08.008.
[12] R. N. Simpson, M. A. Scott, M. Taus, D. C. Thomas, H. Lian, Acoustic isogeometric boundary element analysis, Computer Methods in Applied Mechanics and Engineering 269 (2014) 265–290. doi:10.1016/j.cma.2013.10.026.
[13] H. Lian, R. Simpson, S. Bordas, Stress analysis without meshing: isogeometric boundary element method, Proceedings of the ICE - Engineering and Computational Mechanics 166 (2) (2013) 88–99.
[14] M. A. Scott, R. N. Simpson, J. A. Evans, S. Lipton, S. P. A. Bordas, T. J. R. Hughes, T. W. Sederberg, Isogeometric boundary element analysis using unstructured T-splines, Computer Methods in Applied Mechanics and Engineering 254 (2013) 197–221. doi:10.1016/j.cma.2012.11.001.
[15] H. Lian, P. Kerfriden, S. P. A. Bordas, Implementation of regularized isogeometric boundary element methods for gradient-based shape optimization in two-dimensional linear elasticity, International Journal for Numerical Methods in Engineering (2015) n/a–n/adoi:10.1002/nme.5149.
[16] K. Li, X. Qian, Isogeometric analysis and shape optimization via boundary integral, Computer-Aided Design 43 (11) (2011) 1427–1437. doi:10.1016/j.cad.2011.08.031.
[17] S. Cho, S.-H. Ha, Isogeometric shape design optimization: exact geometry and enhanced sensitivity, Structural and Multidisciplinary Optimization 38 (1) (2008) 53–70. doi:10.1007/s00158-008-0266-z.
[18] G. K. W. Kenway, J. R. R. A. Martins, Multipoint high-fidelity aerostructural optimization of a transport aircraft configuration, Journal of Aircraft 51 (1) (2014) 144–160. doi:10.2514/1.C032150.
[19] L. Piegl, W. Tiller, The NURBS book, Springer Science & Business Media, 2012.
[20] J. A. Cottrell, T. J. R. Hughes, Y. Bazilevs, Isogeometric analysis: Toward integration of CAD and FEA, John Wiley & Sons, 2009.
[21] L. Morino, Boundary integral equations in aerodynamics, Applied Mechanics Reviews 46 (8) (1993) 445–466. doi:10.1115/1.3120373.
[22] E. Klaseboer, C. R. Fernandez, B. C. Khoo, A note on true desingularisation of boundary integral methods for three-dimensional potential problems, Engineering Analysis with Boundary Elements 33 (6) (2009) 796–801. doi:10.1016/j.enganabound.2008.12.002.
[23] J. Katz, A. Plotkin, Low-speed aerodynamics, Cambridge University Press, 2001.
[24] M. Drela, XFOIL: An analysis and design system for low Reynolds number airfoils, in: T. J. Mueller (Ed.), Low Reynolds Number Aerodynamics, no. 54 in Lecture Notes in Engineering, Springer Berlin Heidelberg, 1989, pp. 1–12.
[25] I. H. Abbott, A. E. V. Doenhoff, Theory of wing sections, including a summary of airfoil data, Courier Corporation, 1959.
[26] R. Bouclier, T. Elguedj, A. Combescure, Locking free isogeometric formulations of curved thick beams, Computer Methods in Applied Mechanics and Engineering 245246 (2012) 144–162. doi:10.1016/j.cma.2012.06.008.
[27] A. Cazzani, M. Malagù, E. Turco, Isogeometric analysis of plane-curved beams, Mathematics and Mechanics of Solids (2014) 1081286514531265doi:10.1177/1081286514531265.
[28] A. Beckert, Coupling fluid (CFD) and structural (FE) models using finite interpolation elements, Aerospace Science and Technology 4 (1) (2000) 13–22. doi:10.1016/S1270-9638(00)00111-5.
[29] J. Moran, An introduction to theoretical and computational aerodynamics, John Wiley & Sons, 1984.
[30] H. Squire, A. Young, Air Ministry. Aeronautical Research Committee., The calculation of the profile drag of aerofoils., Aeronautical Research Committee reports and memoranda ; 1838; ARC technical report, HMSO, London, 1937.
[31] G. A. A. Thuwis, Stiffness and layout tailoring of a morphing high-lift system with aeroelastic loads, Ph.D. thesis, Delft University of Technology, Delft (Jun. 2012).
[32] K. Svanberg, A class of globally convergent optimization methods based on conservative convex separable approximations,

SIAM Journal on Optimization 12 (2) (2002) 555–573. doi:10.1137/S1052623499362822.
[33] L. B. Rall, G. Goos, J. Hartmanis, W. Brauer, P. Brinch Hansen, D. Gries, C. Moler, G. Seegmller, J. Stoer, N. Wirth (Eds.), Automatic Differentiation: Techniques and Applications, Vol. 120 of Lecture Notes in Computer Science, Springer Berlin Heidelberg, Berlin, Heidelberg, 1981.

Appendix A

Table 5: Part 1 of the coarse mesh control points and weights for the NACA2412 airfoil

x [m]	y [m]	weight
0.6	0	1
0.596	-0.0003	1
0.5878	-0.0009	1
0.5738	-0.002	1
0.5564	-0.0033	1
0.5346	-0.0049	1
0.5088	-0.0067	1
0.4793	-0.0088	1
0.4467	-0.011	1
0.4115	-0.0133	1
0.3743	-0.0157	1
0.3358	-0.0181	1
0.2967	-0.0203	1
0.2575	-0.0222	1
0.2189	-0.0236	1
0.1817	-0.0248	1
0.1465	-0.0255	1
0.1138	-0.0254	1
0.0842	-0.0245	1
0.0583	-0.0226	1
0.0367	-0.0197	1
0.0197	-0.0157	1
0.0081	-0.0109	1
0.0015	-0.0053	1
-0.0003	0	1

Table 6: Part 2 of the coarse mesh control points and weights for the NACA2412 airfoil

x [m]	y [m]	weight
0.0005	0.0056	1
0.006	0.0124	1
0.0167	0.0193	1
0.033	0.0263	1
0.0542	0.0327	1
0.0799	0.0382	1
0.1096	0.0427	1
0.1426	0.0458	1
0.1784	0.0475	1
0.2161	0.0477	1
0.2552	0.0463	1
0.295	0.0439	1
0.3346	0.0406	1
0.3736	0.0367	1
0.4111	0.0322	1
0.4465	0.0273	1
0.4793	0.0224	1
0.5089	0.0175	1
0.5348	0.0129	1
0.5566	0.0088	1
0.5739	0.0054	1
0.5879	0.0026	1
0.5961	0.0008	1
0.6	0	1